Journal of Electroanalytical Chemistry 878 (2020) 114661

Contents lists available at ScienceDirect

Journal of Electroanalytical Chemistry

journal homepage: www.elsevier.com/locate/jelechem

Formation of active chlorine species involving the higher oxide MO_{x+1} on active Ti/RuO_2-IrO_2 anodes: A DEMS analysis

Mayra Luna-Trujillo [a], Ricardo Palma-Goyes [b,*], Jorge Vazquez-Arenas [c,*], Arturo Manzo-Robledo [a]

[a] Instituto Politecnico Nacional, Laboratorio de Electroquímica y Corrosion, Escuela Superior de Ingeniería Química e Industrias Extractivas (ESIQIE), UPALPM, 07738 Ciudad de Mexico, Mexico
[b] Instituto de Química, Universidad de Antioquia, UdeA, Calle 70 No. 52-21, Medellín, Colombia
[c] Conacyt-Departamento de Química, Universidad Autónoma Metropolitana-Iztapalapa, Av. San Rafael Atlixco No 186, 09340 CDMX, Mexico

ARTICLE INFO

Article history:
Received 18 June 2020
Received in revised form 7 September 2020
Accepted 7 September 2020
Available online 11 September 2020

Keywords:
Ti/RuO_2-IrO_2
Electro-generated active chlorine
Differential electrochemical mass spectroscopy
Surface pH

ABSTRACT

It is accepted that the mechanism of electro-generated active chlorine (i.e. chloride oxidation on DSAs) involves water oxidation and hydroxyl radical co-electrosorption to initially form $HOCl_{ads}$ on the anode surface in a single pathway, and subsequent production of Cl_2 and OCl^- ions. The present study comprehensively evaluates the chloride oxidation on Ti/RuO_2-IrO_2 in solutions containing different NaCl concentrations and pH values. Differential Electrochemical Mass Spectroscopy (DEMS) is used to account for the *in-situ* surface reactions simultaneously occurring during chloride and water oxidations. It is found that HOCl does not lead the chlorine mechanism since $OCl^{\square}$ is detected in considerably larger amounts under some experimental conditions, and its onset overpotential is ~150 mV more negative than HOCl appearance at 0.2 mol L^{-1} NaCl. Additionally, the mass signals of $OCl^{\square}$ and HOCl are virtually similar at pH = 2 and slightly different at pH = 10, where these species should not respectively exist according to thermodynamic information. Under this premise, an extension of the reaction mechanism is proposed to consider an independent pathway producing adsorbed hypochlorite radical ($OCl^{\bullet}_{ads}$) for electro-generated active chlorine, which could be the preferential one since RuO_2 and IrO_2 belong to the category of "active" anodes towards the Oxygen Evolution Reaction (OER), thus allowing the formation of the so-called higher oxide $MO_x(^{\square}O)_{ads}$ (chemisorbed oxygen). Although the mechanisms involving the productions of $HOCl_{ads}$ and $OCl^{\bullet}_{ads}$ can simultaneously occur on two type of non-identified active sites, promoting the generation of both $MO_x(^{\square}OH)_{ads}$ and $MO_x(^{\square}O)_{ads}$ species, both strongly depend on surface pH.

1. Introduction

The redox chemistry of aqueous chlorine species depends on the solution pH, giving place to a distribution of different predominant compounds as described in Fig. 1. Under these experimental conditions, Cl_2 predominates at acidic pH values, while HOCl leads in the range from 2.5 < pH < 7.5, followed by the dominant OCl^- at alkaline conditions. The potential of these redox couples differ from each other: Cl_2/Cl^- E° = 1.36 V vs SHE, $HOCl/Cl^-$ E° = 1.49 V vs SHE and OCl^-/Cl^- E° = 0.89 V vs SHE, whereby they display different oxidation capacities [1].

The discovery of dimensionally stable anodes (DSA) [2], followed by a successful introduction of oxide electrodes (RuO_2 and IrO_2) stimulated the development of durable and catalytic materials to perform chlor-alkali electrolysis [3]. This technology has underpinned over the years, whereby the current research has been encouraged into the synthesis of mixed oxide electrocatalysts to produce electro-generated active chlorine species (Cl_2, HOCl, OCl^-) with high capacity to oxidize various organic and inorganic contaminants including pharmaceutical compounds, pesticides, phenols, nitrite, among others [1,4–11]. The chloride and water oxidation mechanisms occurring on DSA has been previously described in [12–14].

Interestingly, the nature, stability and oxidizing power of these active chlorine species (i.e. adsorbed on the anode surface, electro-generated) contrast against the aforementioned aqueous chlorine species, very stable in solution. In connection with this hypothesis, tremendous efforts have been carried out to synthesize numerous RuO_2-based anodes, by stabilizing the Ru(IV) cations within its crystal lattice using TiO_2, ZrO_2, SnO_2, Ta_2O_5, Nb_2O_5 [11,15–18]. In addition, activity, stability, selectivity and material cost have been remarkably improved. A similar condition has been experienced for IrO_2 phase [19,20], which has been less used due to its higher cost and lower reactivity [21]. These Ru and Ir phases have been used to perform the abatement of recalcitrant organic compounds via electro-generated active chlorine [22,23], which cannot be eliminated from wastewater using typical aqueous chlorine (i.e. hypoclorous acid). Confirming this idea, the destruction of crystal violet was considerably higher when active chlorine was electro-generated on the electrode surface than when directly incorporated as sodium hypochlorite to the solution under alike

* Corresponding authors.
E-mail address: jgva@xanum.uam.mx. (J. Vazquez-Arenas).

http://dx.doi.org/10.1016/j.jelechem.2020.114661

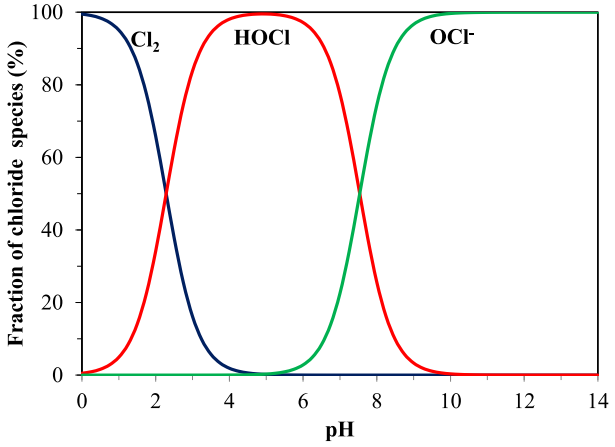

Fig. 1. Fraction of aqueous active chlorine species as a function of pH, calculated using a composition of 0.05 mol L^{-1} NaCl at standard temperature and pressure.

concentration conditions [24]. This draws the attention since similar activities could be expected for these chlorine species presenting analogous structures, thus, suggesting an essential distinction between soluble and electro-generated (adsorbed) active chlorine species. In this direction, De Battisti group theoretically proposed a variation of the mechanism for electrochemical incineration of organics proposed by Comninellis [25], applicable to active chlorine [9]; wherein chloro and oxychloro radicals "co-adsorbed" ($HOCl_{ads}$) on the anode surface are remarked to play important roles on the pollutant mineralization rather than soluble chlorine species, along with the co-electrosorption of hydroxyl radicals.

Recently, Palma et al. conducted experimental studies using DEMS, emphasizing the role of adsorbed species and competing oxygen evolution reaction on Ti/ZrO_2-RuO_2-Sb_2O_3 ternary catalysts of variable composition, revealing that chloride oxidation forms $HOCl_{ads}$ in adequate levels to generate the degradation of organic compounds at pH 5.5, involving the inhibition of the OER [26]. However, this former study was conducted at a single pH value where $HOCl_{ads}$ predominates, whence the proposed reaction mechanism was based on this species. Thus, the formation of electro-generated species arising on a Ti/RuO_2-IrO_2 binary catalyst at different pH values remains unknown, whereby they could be only deducted using thermodynamic information (refer to Fig. 1). Nevertheless, multiple inaccuracies have accompanied these thermodynamic calculations since the reaction mechanisms for electro-generated active chlorine are quite often established using Cl_2 as initial reagent [27–30], regardless of the pH solution. Indeed, these imprecisions preclude a correct interpretation of the kinetic rates and concentrations of the active chlorine species formed on the electrode, affecting experimental measurements and modeling predictions. Thus, the objective of the present work is to experimentally investigate the formation of electro-generated active chlorine species on Ti/RuO_2-IrO_2 (Ti/Ru-Ir) anodes at different NaCl concentrations (0.1 and 0.2 mol L^{-1}), and as a function of pH (2, 7 and 10) for 0.1 mol L^{-1} NaCl. DEMS is used to *in situ* analyze surface electrode reactions through the quantification of molecular weights mass to charge relationship (m/z) of possible ionizable species produced within this mechanism: Cl_2^{70} ($m/z = 70$), $H^1O^{16}Cl^{35}$ ($m/z = 52$), $O^{16}Cl^{35}$ ($m/z = 51$), O_2 [32] ($m/z = 32$) and O^{16} ($m/z = 16$). To this concern, DEMS has become an *in-situ* technique to robustly identify surface products and intermediates of faradaic reactions, characterizing submonolayers of adsorbates on polycrystalline and single crystal electrodes [31]; using the coupling between an electrochemical cell and a conventional mass spectrometer, thus, collecting ionic currents related to the formation of surface species along with the faradaic current during a potential sweep (cyclic voltammetry) [32]. Accordingly, it is expected that this study emphasizes the role of adsorbed chlorine species on the catalytic performance of dimensionally stable anodes, and mainly the strong dependence of this mechanism on surface pH.

2. Experimental

2.1. Synthesis of electrodes

Ti/RuO_2-IrO_2 electrodes were synthesized on titanium plates using the Pechini method according to Palma-Goyes et al. [33]. Analytic grade reagents of $RuCl_{3(aq)}$ and $H_2IrCl_{6\ (aq)}$ were utilized as metallic precursors in a polymeric mixture prepared with a molar ratio of Ru/Ir = 1 with 2.4 mol L^{-1} citric acid as chelating agent, and 18 mol L^{-1} ethylenglycol as reaction solvent. The polymeric mixture was kept stirred for 30 min at 80 °C and subsequently deposited on Ti plates (2 × 2 cm), which were previously treated in oxalic acid at 75 °C for 30 min. These plates were dried at 180 °C for five minutes and calcined at 550 °C for 1 h. Both temperatures were selected from thermogravimetric analysis (TGA) data of the raw polymeric mixture (Supplementary information 1). The coating procedure was repeated eight times to thicken the catalyst. Note that the synthesis method and the substrate guarantee a considerable stability to these electrode materials, as previously reported for comparable structures [33,34], whence they can be used over a considerable amount of cycles.

2.2. Microstructural characterization of anodes

SEM images were collected to determine the morphology of deposited oxide films

using a high-field emission microscope SM-7600F, with accelerating voltage of 10.0 kV. Chemical composition was simultaneously evaluated using Energy-dispersive X-ray spectroscopy (EDS). XRD data were collected with a PANalytical Empyrian diffractometer in a Bragg-Brentano (θ-2θ) configuration operated with a Cu $K_{\alpha1}/K_{\alpha2}$ radiation (λ = 1.5418 Å) at 45 kV and 40 mA from 25 to 60° (2θ) using a PIXcel 3D detector. The crystalline phases were identified using the JCPDS-ICDD cards. The full width at half maximum (FWHM) value for average crystallite size (i.e. Scherrer equation) was obtained from a profile refinement using the FULLPROF program.

2.3. Electrochemical analysis

Linear sweep voltammetry (LSV) was conducted with an Autolab PGSTAT 302 N potentiostat/galvanostat in an electrolyte containing different NaCl (Merck ≥99.0%) concentrations (0.1 and 0.2 mol L^{-1}, pH values of 6.5 and 6.3, respectively) using a scan rate of 1 mV s^{-1} at room temperature. The pH variation as a function of NaCl concentration could be due to traces of anions, cations and other impurities contained in the chemical reagent. A three-electrode cell was used to carry out these electrochemical experiments. DSA (Ti/RuO_2-IrO_2, geometric area of 0.0706 cm^2) and hydrogen electrode (RHE) were used as working and reference electrodes, respectively; and a pure graphite rod (Alfa AESAR, 99.997%) as counter electrode.

2.4. Differential electrochemical mass spectrometry

The cell to conduct the DEMS measurements was connected to the chamber containing the quadropole mass spectrometer (MS) with a Faraday-SEM detector array (Prisma QMG 200, Pfeiffer), which allows the isolation of the ion source from the electrochemical cell forming a small pre-chamber. A turbomolecular pump evacuates the latter, whereas the vacuum in the chamber containing the MS is obtained from another turbomolecular pump. The amount of species reaching the MS can be controlled with another dosing valve located between the electrochemical cell and the pre-chamber. A simple DEMS cell based on a reported design was built for the use of massive electrodes [35]. The interface between the cell and the vacuum consists of a porous Teflon membrane (60 μm thick, 0.2 μm pore diameter, 75% porosity). A conventional three-electrode arrangement was employed for the electrochemical measurements (Supplementary information 2). A reference hydrogen electrode (RHE) was prepared in the supporting electrolyte and a graphite rod served as the

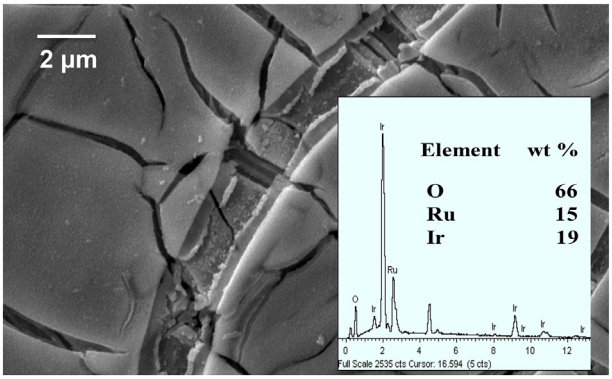

Fig. 2. Scanning Electron Microscopy images collected for the Ti/RuO_2-IrO_2 anode. EDS analysis of the sample is shown as inset.

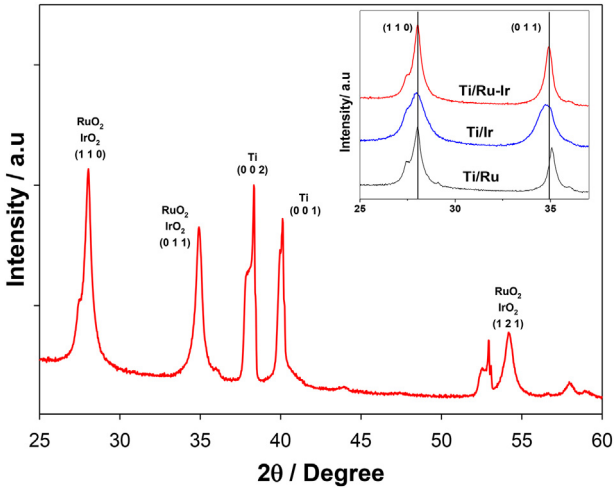

Fig. 3. X-ray diffraction patterns collected from the Ti/RuO_2-IrO_2 anode in the range from 25 to 60 degrees (2θ). Inset. X-ray diffraction patterns collected from Ti/RuO_2(Ti/Ru), Ti/IrO_2 (Ti/Ir) and Ti/RuO_2-IrO_2 (Ti/Ru-Ir).

counter-electrode. The working electrode was located next to the Teflon membrane, and DEMS experiments were carried out. Mass spectrometric cyclic voltammograms (MSCVs) for selected mass to charge ratios (m/z) were recorded for the following ionizable species: Cl_2^{70} (m/z = 70), $H^1O^{16}Cl^{35}$ (m/z = 52), $O^{16}Cl^{35}$ (m/z = 51), O_2 [32] (m/z = 32) and O^{16} (m/z = 16). Similar volatile and structural ionizable compounds have been detected in previous studies involving radical species [26,36]. Acceptable time responses were obtained with this configuration for scan rates of 1 mV s^{-1}. The working pressure in the main chamber was kept constant at ca. 6 × 10^{-6} mbar for all the experiments. Each set of experiments was repeated at least twice to ensure reproducibility.

3. Results and discussions

3.1. Microstructural characterization

Fig. 2 describes SEM images of the Ti/RuO_2-IrO_2 electrode, where the formation of mud-cracked structures with flat areas is evident on the catalyst surface. This type of morphology is presumably formed during the calcination stage of the anode material (i.e. solvent and water evaporations) [37,38]. Albeit these morphological features could not be desired in the surface of a catalyst, it brings great benefits associated with the non-accumulation of species resulting from chlorine evolution (i.e. Cl_2), and other reactions promoting the loss of adherence between the substrate and the catalyst film. The EDS analysis performed on the DSA (inset of Fig. 2) accounts for weight ratios in the range of the oxide stoichiometry: 66, 15 and 19 wt% for O, Ru and Ir, respectively.

Fig. 3 shows the X-Ray diffraction analysis for the binary Ti/Ru-Ir electrode, where a new phase of Ru and Ir metallic oxides was effectively synthesized on a rutile (TiO_2) layer (JCPDS 00–9161), earlier formed on Ti substrate (04–3416). The presence of metallic Ti (JCPDS 04–316) was connected with the substrate. The formation of the RuO_2-IrO_2 crystal is possible since Ir and Ru present similar cationic radius, and their oxides exhibit a rutile-type crystal structure [39], whereby their lattice parameters are analogous, RuO_2 (JCPDS 05–1159) and IrO_2 (JCPDS 08–4577). The Ru-Ir crystal structure was assigned to tetragonal rutile ($P4_2/mmm$): 2θ = 28, 35 and 54° attributed to (1 1 0), (0 1 1) and (1 2 1) reflection planes, respectively. Accordingly, the TiO_2 substrate can orient the RuO_2 and IrO_2 growths. In this direction, a gradual shift is registered for the (110) peak located at 28° for the mixed oxide (Fig. 3), indicating a lattice modification resulting from the synthesis of a single phase. Raman spectroscopy (Supplementary information 3) confirmed that the mixed Ti/Ru-Ir catalyst only showed two broad signals close to 538 (E_g) and 706 cm^{-1} (B_{2g} and A_{1g}). The gradual shift of the E_g band with respect to pure Ru (E_g = 516 cm^{-1}) and Ir (E_g = 548 cm^{-1}) [40], and no splitting for the A_{1g} and B_{2g} bands may indicate a lattice modification and the formation of metal oxide particles with substitution of Ir by Ru atoms in the rutile structure [41,42]. According to Hume–Rothery theory, this ternary oxide system can form a solid solution [43], since the ionic radius of Ru^{4+} (0.076 nm), Ir^{4+} (0.077 nm) and Ti^{4+} (0.075 nm) are similar and these oxides display rutile-type structures. Supplementary information 4 describes the profile refinement fitting conducted for the Ti/Ru-Ir electrode for a more detailed analysis of its microstructure. The average crystallite size for this electrode was calculated through Scherrer equation:

$$\tau = \frac{0.9\lambda}{\beta \cos\theta} \quad (1)$$

where τ is the mean grain size, λ is the X-ray wavelength, β is the full-width at half maximum (FWHM) and θ is the Bragg's angle. The FWHM was determined via Caglioti function using the U, V, W peak shape functions obtained from the refinement, previous instrumental correction with a LaB6 NIST standard. Results obtained from Scherrer equation reveal an average crystallite size of 12 nm for this catalyst.

3.2. Electrochemical studies and DEMS analysis

The first idea to confirm a distinction between soluble and adsorbed chlorine species could be based on the monitoring of their activity towards the degradation of an organic recalcitrant compound. In this regard, Fig. 6 of our former study reported in ref. [24] presented the decays of concentration and total organic carbon (TOC) during the electrochemical (Ti/RuO_2-IrO_2) and chemical oxidations of 614 μmol L^{-1} Crystal Violet at pH 6.4. The chemical oxidation was conducted with 1 mol L^{-1} of hypoclorous acid (HOCl), while electrolysis was performed at 15 mA cm^{-2} on Ti/RuO_2-IrO_2 in 0.1 mol L^{-1} NaCl. Note that according to the Fraction-pH diagram shown in Fig. 1, the same chlorine species (HOCl) predominates at this pH value. Interestingly, the drop of Crystal Violet concentration proceeds considerably faster in the electrochemical process than the chemical one, even when the latter one employed a higher concentration of chlorine species (1 mol L^{-1} of hypoclorous acid). In the same way, the electrochemical process electro-generating adsorbed chlorine species produces an important mineralization of the dye as verified in the TOC depletion, while it remains at very reduced states when aqueous chlorine species are used in the chemical method. Additional tests were described to verify that direct electrochemical oxidation of Crystal Violet was not occurring during the oxidation via active chlorine species shown in supplementary data 5 [24]. From these results, there is sufficient evidence to assume that electro-generated active chlorine species (Cl_{2ads}, $HOCl_{ads}$, OCl^-_{ads}) generate a higher oxidizing power compared to their parental soluble chlorine (Cl_2, HOCl, OCl^-), very stable in solution. This reactivity analysis enables

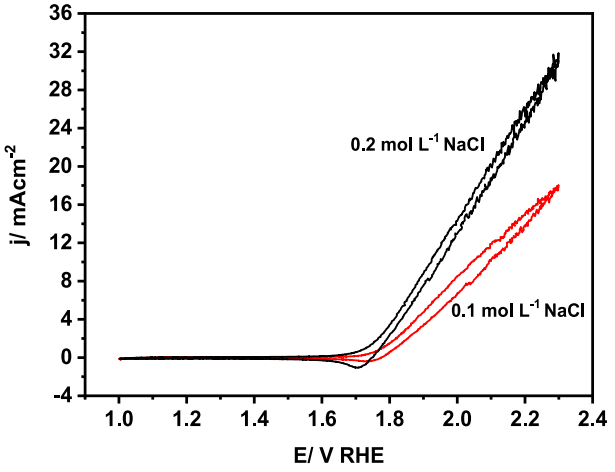

Fig. 4. Cyclic voltammograms collected at different NaCl concentrations (0.1 and 0.2 mol L^{-1}) on a Ti/RuO_2-IrO_2 anode using 1 mV s^{-1}.

a better conceptualization of the adsorbed species formed on Ti/RuO_2-IrO_2 during chloride oxidation described in the following experiments.

Fig. 4 displays typical cyclic voltammograms collected at different NaCl concentrations (0.1 and 0.2 mol L^{-1}, pH values of 6.5 and 6.3, respectively) on a Ti/RuO_2-IrO_2 anode at 1 mV s^{-1}. The scan was started in the anodic direction and switched back to the cathodic region. It is evident that chloride oxidation mainly occurs on this electrode since the current density remarkably increases with chloride concentration. The onset of this reaction occurs around 1.7 V vs. RHE, where the current starts rising, denoting that chloride oxidation is the main faradaic reaction in the system. When the potential scan is inverted to the cathodic direction, a wave around 1.7 V vs. RHE indicates the reduction of the previously formed chlorine species on the electrode surface (i.e. adsorbed), being also a function of the NaCl concentration. As observed in Fig. 4, the highest anodic current density is produced at 0.2 mol L^{-1}, also indicating the largest production of active chlorine species if compared against the voltammogram obtained at 0.1 mol L^{-1}, regardless of the OER contributions. This result is confirmed in the backward scan, where chlorine species are reduced, thus, producing the highest cathodic current at 0.2 mol L^{-1}. Note that the anodic and cathodic waves strongly depend on the ohmic drop, as detected in the shifts of the electrochemical processes towards more positive potentials observed for the lowest concentration (0.1 M NaCl).

In order to monitor the electro-generation of active chlorine species, voltammograms and DEMS-based signals (ionic current versus potential) were simultaneously collected on a Ti/RuO_2-IrO_2 anode in solutions containing different concentrations of NaCl (0.1 and 0.2 mol L^{-1}, pH values of 6.5 and 6.3, respectively) and 0.1 M $NaClO_4$ (pH 6.4). The following mass spectrometric ion currents signals (MSCV) of possible ionizable species evolved during electrolysis were collected: Cl_2^{70} (m/z = 70), $H^1O^{16}Cl^{35}$ (m/z = 52), $O^{16}Cl^{35}$ (m/z = 51), O_2 [32] (m/z = 32) and O^{16} (m/z = 16). The O^{16} signals in Figs. 5 and 6 resemble the corresponding ionic currents of O_2 [32], strongly depending on the electrolyte ($NaClO_4$ and NaCl) and the magnitudes of ionic currents, thus, indicating O^{16} results from the electron bombardment in the quadropole mass spectrometer of O_2 species [32]. On the other hand, this behavior is not presented with the $O^{16}Cl^{35}$ species described in the same figures, which even exceed the ionic currents of $H^1O^{16}Cl^{35}$ and Cl_2^{70}. Additionally, $O^{16}Cl^{35}$ species appear in the potential scan right before any other species whereby it cannot result from the fragmentation of other compounds. DEMS is subjected to high vacuum at low pressure, whereby it is able to detect a small disturbance-variation of volatile or dilute species with low vapor pressure generated or consumed during surface reactions, even being very dilute species. Fig. 5 shows typical voltammetry tests (OCP ≈ 1 to 2.3 V vs RHE using 1 mV s^{-1} as scan rate) and their respective ionic signals measured in 0.1 mol L^{-1} $NaClO_4$, to evaluate the oxygen evolution reaction (OER) in a chloride-free solution. The voltammogram is characterized by a large overpotential up to 1.7 V vs RHE, where an electrochemical reaction starts. As observed, the corresponding signals Cl_2^{70}, $H^1O^{16}Cl^{35}$ and $O^{16}Cl^{35}$ species are not virtually detected, and the only observable signals at the onset current (~1.7 V) are associated with oxygen (O_2 [32] and O^{16}). Not surprisingly, chloride oxidation does not occur in the system since there is not free chloride in the solution, thus, only the OER proceeds on the electrode. When NaCl (0.1–0.2 mol L^{-1}) is considered in the bath, the first observation is that OER is considerably suppressed due to the occurrence of chloride oxidation, although this parasitic reaction still persists in considerable amounts in the range of 10^{-9} A, also confirming its predecessor role to produce $^{\bullet}OH$. Nevertheless, this finding confirms that the Ti/RuO_2-IrO_2 electrocatalyst is particularly active to generate adsorbed chlorine from the OER suppression. A similar result has been reported by

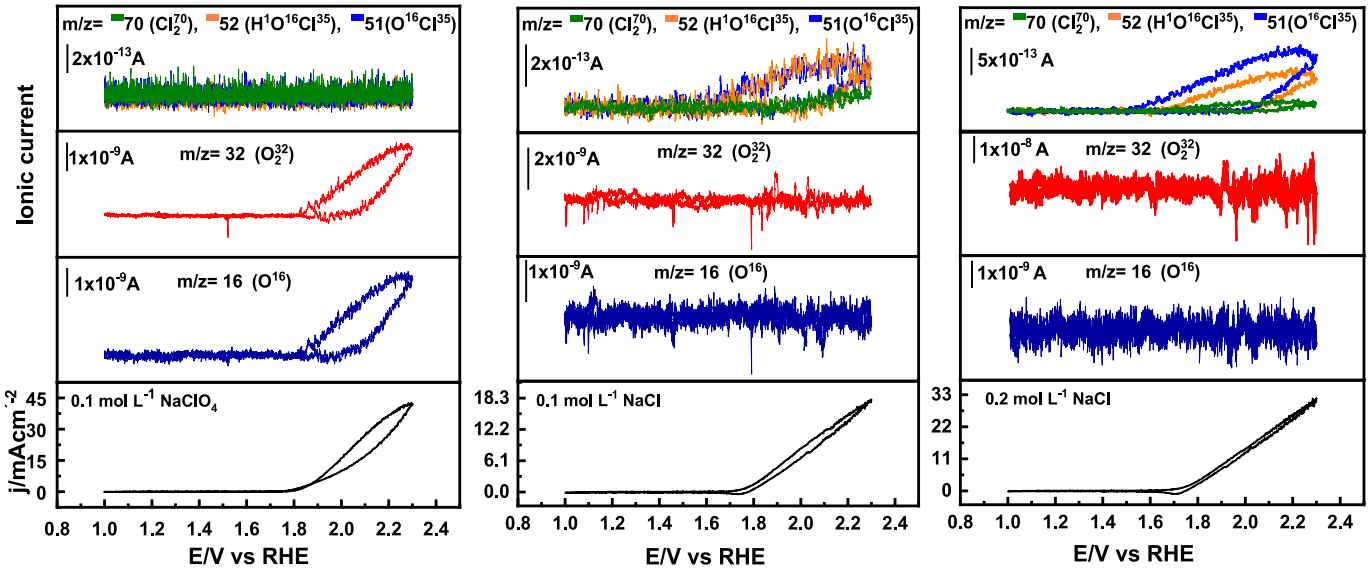

Fig. 5. Voltammograms and DEMS-based signals of Cl_2^{70} (m/z = 70), $H^1O^{16}Cl^{35}$ (m/z = 52), $O^{16}Cl^{35}$ (m/z = 51), O_2 [32] (m/z = 32) and O^{16} (m/z = 16) as a function of applied potential recorded during the chloride oxidation on Ti/RuO_2-IrO_2 electrodes at different $NaClO_4$ (0.1 mol L^{-1}) and NaCl (0.1 and 0.2 mol L^{-1}) concentrations. Scan rate: 1 mV s^{-1}.

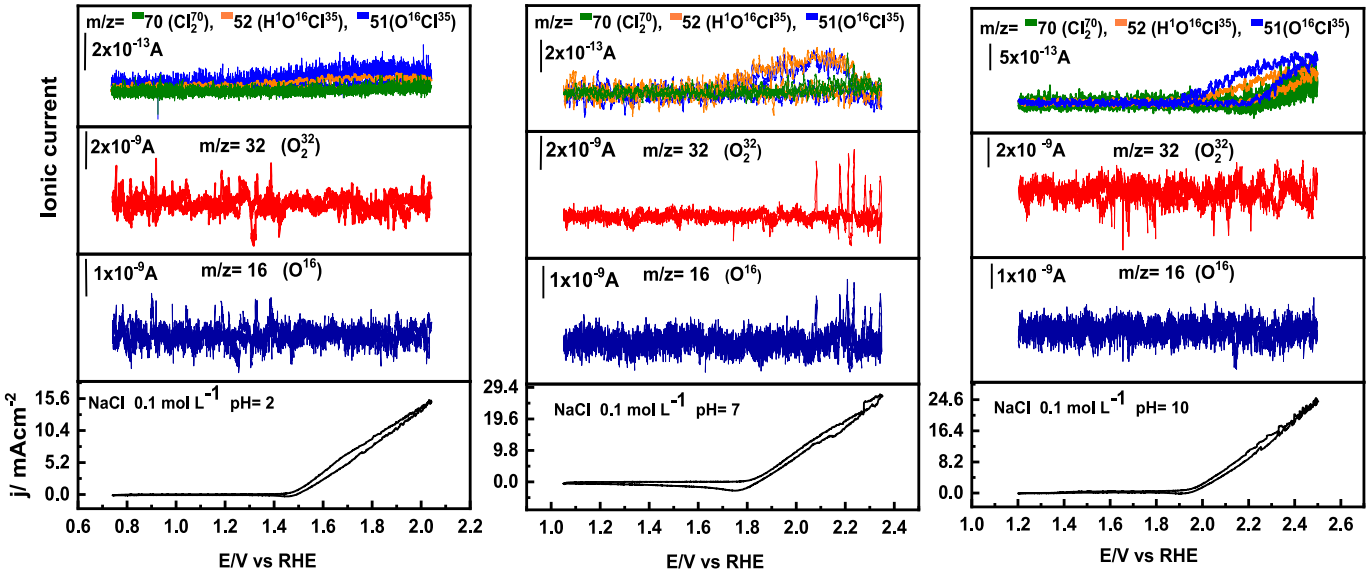

Fig. 6. Voltammograms and DEMS-based signals of Cl_2^{70} (m/z = 70), $H^1O^{16}Cl^{35}$ (m/z = 52), $O^{16}Cl^{35}$ (m/z = 51), O_2 [32] (m/z = 32) and O^{16} (m/z = 16) as a function of applied potential recorded during the chloride oxidation on Ti/RuO_2-IrO_2 electrodes at 0.1 mol L^{-1} and different pH values (2, 7 and 10). Scan rate: 1 mV s^{-1}.

Palma et al. on a Ti/RuO_2-ZrO_2-Sb_2O_3 electrode [26]. The mass signals are clearly observed at 0.1 mol L^{-1} NaCl due to the significant concentrations produced for active chlorine species (Fig. 5). Note that the ionic currents related to $H^1O^{16}Cl^{35}$ and $O^{16}Cl^{35}$ are slightly higher compared to Cl_2^{70}. These mass signals are remarkably increased at 0.2 mol L^{-1} NaCl (Fig. 5), wherein $O^{16}Cl^{35}$ presents the highest ionic current followed by $H^1O^{16}Cl^{35}$ and then Cl_2^{70}. Surprisingly, this trend does not follow the results described by the thermodynamic fraction-pH diagram shown in Fig. 1 around this pH (6.5–6.3), where HOCl is the predominating species followed by $O^{16}Cl^{35}$. Additionally, the onset overpotential to form $O^{16}Cl^{35}$ is located approximately 150 mV more negative than $H^1O^{16}Cl^{35}$ and Cl_2^{70} at this concentration. These particular findings indicate that for this electrode (Ti/RuO_2-IrO_2), $H^1O^{16}Cl^{35}$ could not be an initial requirement to form $O^{16}Cl^{35}$, since the mass signal of this last species is considerably higher compared to $H^1O^{16}Cl^{35}$ in Fig. 5 (0.2 mol L^{-1} NaCl), and its appearance occurs at considerable more negative potentials. A similar situation arises for Cl_2^{70}, which presents some mass signal under this condition (Fig. 5, 0.1 and 0.2 mol L^{-1} NaCl), in a region where its co-existence (pH 6.5–6.3) has almost vanished as presented in the thermodynamic diagram in Fig. 1. Although the course of LSVs (i.e. total length of experiment) shown in Fig. 5 could be considered as moderate, the scan rate is low (i.e. close to equilibrium conditions) enabling the mass transport to the electrode surface through the membrane, without completely depleting H_2O or chloride species on the DSA. Under this assumption, it is expected that the time domains of transport through the membrane for these species are faster, than those required for mass transport within the boundary layer nearby the anode surface or the electrochemical reactions. Thus, the system particularly proceeds under mixed control at large overpotentials, without being affected by the mass transport of electroactive species through the Teflon membrane.

Fig. 6 presents the effect of pH variation when the NaCl concentration is maintained constant at 0.1 mol L^{-1}. As observed, there is again an important inhibition of OER due to the catalysis of chloride oxidation, as described in ref. [26]. At pH 2, the highest mass signal is once more detected for $O^{16}Cl^{35}$ as previously described in Fig. 5, followed very close by the ionic currents for $H^1O^{16}Cl^{35}$ and then Cl_2^{70}. This kinetic behavior contradicts the thermodynamic information reported in Fig. 1, where Cl_2^{70} is the predominating species around acidic pH value. When a pH equals 7 is considered in the experiment (Fig. 6), the thermodynamic diagram agrees with the mass signals detected for chlorine species since the highest detection is obtained for $H^1O^{16}Cl^{35}$, followed very close by $O^{16}Cl^{35}$ and then Cl_2^{70}. Likewise, an agreement between kinetics and thermodynamics is again perceived in Fig. 6 (pH = 10), where $O^{16}Cl^{35}$ displays the highest ionic current and there is some formation of HOCl. The onset overpotential of $O^{16}Cl^{35}$ is again slightly more negative compared to HOCl. However, it is surprising to observe the yield of Cl_2^{70} since the thermodynamic diagram reveals a null coexistence under alkaline conditions. This deviation from the thermodynamic information obtained during electrode kinetics could be related to changes in the interfacial conditions (H^+ and chloride concentrations) compared to the bulk solution. In fact, it has been concluded that the mechanism of Cl_2 evolution on oxide electrodes is complex due to the pH dependence on surface charging (i.e. surface specific features) [12]. It is worthwhile mentioning that the changes observed in Figs. 5 and 6 are not only due to significant variations between bulk and interfacial pH values, which otherwise nullify the significant formation of co-existing species according to thermodynamic stability (e.g. appearance of $O^{16}Cl^{35}$ at pH = 2 and Cl_2^{70} at pH = 10); but might also indicate changes in the reaction mechanism induced by the possible existence of more than one type of active site and variations in the interfacial pH.

The following points summarized the above findings and related literature:

1. Since Both RuO_2 and IrO_2 belong to the category of "active" anodes (i.e. those able to form the so-called higher oxide MO_{x+1}), also the Ti/RuO_2-IrO_2 electrode is expected to allow the formation of $MO_x(^{\bullet}O)_{ads}$ (chemisorbed oxygen); on the other hand, only $MO_x(^{\bullet}OH)_{ads}$ species (i.e. physisorbed oxygen) can form on "non-active" anodes like Ti/SnO_2-Pt and Ti/PbO_2 [9].
2. At high chloride concentrations (pH ≈ 6.5, Fig. 5) where HOCl thermodynamically predominates, $O^{16}Cl^{35}$ is detected by DEMS in larger amounts than any other active chlorine species.
3. Cl_2^{70} is always generated in lower amounts compared to other chlorine species, whereby its mass signal is somehow correlated to $H^1O^{16}Cl^{35}$ and $O^{16}Cl^{35}$, possibly indicating connected pathways.
4. The mass signals of $O^{16}Cl^{35}$ and $H^1O^{16}Cl^{35}$ are approximately similar at pH = 2 and slightly different at pH = 10, where $^{\bullet}$OCl and HOCl should not exist according to the thermodynamic information, respectively.
5. $H^1O^{16}Cl^{35}$ cannot precede the formation of all chlorine species as proposed for Ti/PbO_2 and Ti/SnO_2-Pt [9], since these two last species can be generated under certain conditions described in Figs. 5 and 6 in considerably larger concentrations. Likewise, the onset overpotential to form $O^{16}Cl^{35}$ is approximately 150 mV more negative than $H^1O^{16}Cl^{35}$ and Cl_2^{70} at 0.2 mol L^{-1} NaCl.

6. There is an important inhibition of OER in the presence of chloride oxidation.

According to the above experimental evidence, we propose an extension for the reaction mechanism of electro-generated active chlorine [9], specifically occurring on Ti/RuO_2-IrO_2 at acidic conditions, considering the following identification of the species detected by DEMS, Cl_2^{70} (**Cl_2**), $H^1O^{16}Cl^{35}$ (**HOCl**) and $O^{16}Cl^{35}$ ($^{\bullet}$OCl):

$$MO_x + H_2O_{(l)} \rightarrow MO_x(H_2O)_{ads} \quad (1)$$

$$MO_x(H_2O)_{ads} \rightarrow MO_x\left(^{\bullet}OH\right)_{ads} + H^+_{(aq)} + e^- \quad (2)$$

$$MO_x\left(^{\bullet}OH\right)_{ads} + Cl^-_{(aq)} \rightarrow MO_x(\mathbf{HOCl})_{\boldsymbol{ads}} + e^- \quad (3a)$$

$$MO_x(\mathbf{HOCl})_{\boldsymbol{ads}} + Cl^-_{(aq)} \rightarrow MO_x + \boldsymbol{Cl_2}(\boldsymbol{g}) + OH^- \quad (4a)$$

$$MO_x\left(^{\bullet}OH\right)_{ads} \rightarrow MO_x\left(^{\bullet}O\right)_{ads} + H^+_{(ac)} + e^- \quad (3)$$

$$MO_x\left(^{\bullet}O\right)_{ads} + Cl^-_{(aq)} \rightarrow MO_x\left(^{\bullet}\mathbf{OCl}\right)_{\boldsymbol{ads}} + e^- \quad (4b)$$

$$MO_x\left(^{\bullet}\mathbf{OCl}\right)_{\boldsymbol{ads}} + Cl^-_{(aq)} \rightarrow MO_x\left(^{\bullet}O\right)_{ads} + \boldsymbol{Cl_2}(\boldsymbol{g}) + e^- \quad (5b)$$

$$MO_x\left(^{\bullet}O\right)_{ads} + H_2O_{(l)} \rightarrow MO_x\left(^{\bullet}OOH\right)_{ads} + H^+_{(ac)} + e^- \quad (4)$$

$$MO_x\left(^{\bullet}OOH\right)_{ads} \rightarrow M(\mathbf{O_2})_{\boldsymbol{ads}} + H^+_{(ac)} + e^- \quad (5)$$

Chemical equilibria in solution

$$Cl_2 + H_2O \leftrightarrow HOCl_{(aq)} + Cl^-_{(aq)} + H^+_{(aq)}\ pK = 3.29 \quad (6)$$

$$HOCl_{(aq)} \leftrightarrow ClO^-_{(aq)} + H^+_{(aq)}\ pK = 7.54 \quad (7)$$

where MO_x accounts for an active site on an oxygen atom of the electrocatalyst surface, and $X_{(ads)}$ an adsorbed intermediate species on MO_x. Reactions in black denote the typical OER inhibited on Ti/RuO_2-IrO_2 (Figs. 5 and 6), and involving the adsorption of hydroxyl radical (reaction 2). The occurrence of this mechanism is justified due to the presence of O_2 (reaction 5) in Figs. 5 and 6, regardless it is inhibited by the independent formation of active chlorine species (reactions 3a and 4b). Additionally, the voltammograms shown in these plots reveal that single chloride species would not be able to sustain the high current observed at large overpotentials, otherwise, the current would drop due to its mass transport control. This current decay is not observed in these experiments indicating that the current is also made up from contributions of the OER. Reactions highlighted in grey (3a and 4a) describe the mechanism to produce adsorbed HOCl using $^{\bullet}$OH as active site, according to different studies in the literature [9,44]. However, reactions (3a and 4a) and (6–7) cannot be the main route to form Cl_2 and $^{\bullet}$OCl under some of the conditions of our study, according to the explanations provided above for Figs. 5 and 6. We believe that the electrocatalyst surface can contain at least two type of active sites (e.g. MO_x) promoting the generation of both $MO_x(^{\bullet}OH)_{ads}$ and $MO_x(^{\bullet}O)_{ads}$ species (reactions 4b-5b highlighted on red) where Cl^- ions can be oxidized, and they are strongly favored with pH. This proposal is based on the fact that HOCl and $^{\bullet}$OCl occur in similar concentrations, regardless of the NaCl concentration (Fig. 5) and pH (Fig. 6). Note that for neutral and alkaline conditions, water hydrolysis ($H_2O_{(l)} \rightarrow H^+_{aq)} + OH^-_{(aq)}$) needs to be added to the mechanism described by reactions (1–7). This diversity of the reaction mechanism could be due to the presence of different phases on the electrode surface or planes (110, 011, 121) as described in the XRD analysis. However, we have not conclusive results concerning this aspect due to the complexity involved to evaluate the relationship established between structure and activity. Under this condition, $^{\bullet}$OCl is primarily formed at high NaCl concentrations and alkaline pH values, remarking the pH dependence on surface charging of the active chlorine mechanism [12]. Reaction (4b) is a more direct pathway to consider oxygen surface sites to discharge Cl^- in order to produce adsorbed $^{\bullet}$OCl on the electrode. A subsequent chloride oxidation as described by reaction (5b) can form the Cl_2. Thus, the reaction mechanism described by reactions (4b-5b) is complementary to the former mechanism (3a-4a) proposed in ref. [9], assigning a more important role to the $HOCl_{ads}$ formation. Different concentration values can be expected by altering the local pH, and then the concentration and presence of HClO and $^{\bullet}$OCl in most of the solution on the anode surface [45], the latter probably affected by mass transfer kinetics and current density. Under this premise, the electrode surface plays a more important role in the catalytic mechanism while maintaining a consistency of the pH conditions. This mechanism (reactions 4b-5b) is similar to the one theoretically proposed by Janssen et al. [46] and Burke and O'Neill [47] with the difference that water oxidation and hydroxyl radical co-electrosorption adopt decisive roles in the reaction pathway.

4. Conclusions

A dimensionally stable anode of Ti/RuO_2-IrO_2 was synthesized via the Pechini method, morphologically characterized by SEM, XRD and Raman, and electrochemically evaluated using *in situ* DEMS measurements to account for the surface reaction mechanism of electro-generated active chlorine as a function of pH. Mass spectrometric ion currents signals of possible volatile species formed during chloride electrolysis were collected: Cl_2^{70} (m/z = 70), $H^1O^{16}Cl^{35}$ (m/z = 52), $O^{16}Cl^{35}$ (m/z = 51), O_2 [32] (m/z = 32) and O^{16} (m/z = 16). Electrolytes at different NaCl concentrations and pH values were used for these purposes.

An extension of the reaction mechanism for electro-generated active chlorine (i.e. $^{\bullet}$OCl formation pathway) involving water oxidation and hydroxyl radical co-electrosorption was proposed to explain the following kinetic information evaluated using DEMS: a) Cl_2^{70} was always generated in lower amounts compared to other chlorine species, whereby its mass signal was somehow correlated to $H^1O^{16}Cl^{35}$ and $O^{16}Cl^{35}$, b) $O^{16}Cl^{35}$ was detected in larger amounts than any other active chlorine species at high chloride concentrations (pH ≈ 6.5) where HOCl thermodynamically predominated, c) $H^1O^{16}Cl^{35}$ could not precede the formation $O^{16}Cl^{35}$ since this species was generated in considerably larger concentrations under certain conditions, and the onset overpotential to form it was approximately 150 mV more negative than HOCl at 0.2 mol L^{-1} NaCl, d) the mass signals of $O^{16}Cl^{35}$ and $H^1O^{16}Cl^{35}$ were approximately similar at pH = 2 and slightly different at pH = 10, where $O^{16}Cl^{35}$ and $H^1O^{16}Cl^{35}$ should not exist according to the thermodynamic information, respectively, and e) there was an important inhibition of OER in the presence of chloride oxidation. Albeit the mechanisms involving the formation of $HOCl_{ads}$ and $^{\bullet}OCl_{ads}$ could simultaneously occur, the main oxidation pathway could be associated with $MO_x(^{\bullet}OCl)_{ads}$, based on the fact that "active" anodes are able to stabilize chemisorbed oxygen through the formation of $MO_x(^{\bullet}O)_{ads}$ species, while the less stable physisorbed species $MO_x(^{\bullet}OH)_{ads}$ and $MO_x(HOCl)_{ads}$ are the prerogative of "non-active" anodes. However, it was suggested that the electrocatalyst surface could contain at least two type of non-identified active sites, promoting the generation of both $MO_x(^{\bullet}OH)_{ads}$ and $MO_x(^{\bullet}O)_{ads}$ species where Cl^- ions can be concurrently oxidized. This proposal was based on the fact that HOCl and $^{\bullet}$OCl arose in similar concentrations, regardless of the NaCl concentration and bulk pH. Further complex studies needs to be conducted to determine the identity of these active sites.

Declaration of Competing Interest

There are no conflicts to declare.

Acknowledgments

An especial acknowledgement is dedicated to the unknown reviewer who made comments and suggestions that remarkably improved this paper. Financial support was provided by SECTEI-CDMX-MEXICO (grant CM 289/2019), SIP-IPN (grant no. 20200352), and Ciencia Básica CONACYT 2018 grant no. A1-S-21608. AMR thanks DEMS projects 160333, 247208 and IPN 20200507, 20195212.

Appendix A. Supplementary data

Supplementary data to this article can be found online at https://doi.org/10.1016/j.jelechem.2020.114661.

References

[1] M. Deborde, U. Von Gunten, Reactions of chlorine with inorganic and organic compounds during water treatment—kinetics and mechanisms: a critical review, Water Res. 42 (2008) 13–51.
[2] H.B. Beer, The invention and industrial development of metal anodes, J. Electrochem. Soc. 127 (1980) 303C–307C.
[3] S. Trasatti, Electrocatalysis: understanding the success of DSA®, Electrochim. Acta 45 (2000) 2377–2385.
[4] H. Gallard, U. von Gunten, Chlorination of phenols: kinetics and formation of chloroform, Environ. Sci. Technol. 36 (2002) 884–890.
[5] Y. Magara, T. Aizawa, N. Matumoto, F. Souna, Degradation of pesticides by chlorination during water purification, Water Sci. Technol. 30 (1994) 119.
[6] D.W. Johnson, D.W. Margerum, Non-metal redox kinetics: a reexamination of the mechanism of the reaction between hypochlorite and nitrite ions, Inorg. Chem. 30 (1991) 4845–4851.
[7] S.E. Duirk, T.W. Collette, Degradation of chlorpyrifos in aqueous chlorine solutions: pathways, kinetics, and modeling, Environ. Sci. Technol. 40 (2006) 546–551.
[8] L.K. Folkes, L.P. Candeias, P. Wardman, Kinetics and mechanisms of hypochlorous acid reactions, Arch. Biochem. Biophys. 323 (1995) 120–126.
[9] F. Bonfatti, S. Ferro, F. Lavezzo, M. Malacarne, G. Lodi, A. De Battisti, Electrochemical incineration of glucose as a model organic substrate. II. Role of active chlorine mediation, J. Electrochem. Soc. 147 (2000) 592–596.
[10] F. Bonfatti, A. De Battisti, S. Ferro, G. Lodi, S. Osti, Anodic mineralization of organic substrates in chloride-containing aqueous media, Electrochim. Acta 46 (2000) 305–314.
[11] M. Panizza, G. Cerisola, Electrochemical oxidation of 2-naphthol with in situ electrogenerated active chlorine, Electrochim. Acta 48 (2003) 1515–1519.
[12] S. Trasatti, Progress in the understanding of the mechanism of chlorine evolution at oxide electrodes, Electrochim. Acta 32 (1987) 369–382.
[13] M. Tahir, L. Pan, F. Idrees, X. Zhang, L. Wang, J.-J. Zou, Z.L. Wang, Electrocatalytic oxygen evolution reaction for energy conversion and storage: a comprehensive review, Nano Energy 37 (2017) 136–157.
[14] M. Busch, Water oxidation: From mechanisms to limitations, Curr. Opin. Electrochem. 9 (2018) 278–284.
[15] R. Chen, V. Trieu, B. Schley, H. Natter, J. Kintrup, A. Bulan, R. Weber, R. Hempelmann, Anodic electrocatalytic coatings for electrolytic chlorine production: a review, Z. Phys. Chem. 227 (2013) 651–666.
[16] Y. Takasu, W. Sugimoto, Y. Nishiki, S. Nakamatsu, Structural analyses of RuO 2–TiO 2/Ti and IrO 2–RuO 2–TiO 2/Ti anodes used in industrial chlor-alkali membrane processes, J. Appl. Electrochem. 40 (2010) 1789–1795.
[17] J. Gaudet, A. Tavares, S. Trasatti, D. Guay, Physicochemical characterization of mixed RuO2− SnO2 solid solutions, Chem. Mater. 17 (2005) 1570–1579.
[18] S. Chen, Y. Zheng, S. Wang, X. Chen, Ti/RuO2–Sb2O5–SnO2 electrodes for chlorine evolution from seawater, Chem. Eng. J. 172 (2011) 47–51.
[19] R.E. Palma-Goyes, J. Silva-Agredo, J. Vazquez-Arenas, I. Romero-Ibarra, R.A. Torres-Palma, The effect of different operational parameters on the electrooxidation of indigo carmine on Ti/IrO2-SnO2-Sb2O3, J. Environ. Chem. Eng. 6 (2018) 3010–3017.
[20] R.A. Herrada, G. Acosta-Santoyo, S. Sepúlveda-Guzmán, E. Brillas, I. Sirés, E. Bustos, IrO2-Ta2O5| Ti electrodes prepared by electrodeposition from different Ir: Ta ratios for the degradation of polycyclic aromatic hydrocarbons, Electrochim. Acta 263 (2018) 353–361.
[21] T. Le Luu, J. Kim, J. Yoon, Physicochemical properties of RuO2 and IrO2 electrodes affecting chlorine evolutions, J. Ind. Eng. Chem. 21 (2015) 400–404.
[22] A. Perea, R.E. Palma-Goyes, J. Vazquez-Arenas, I. Romero-Ibarra, C. Ostos, R.A. Torres-Palma, Efficient cephalexin degradation using active chlorine produced on ruthenium and iridium oxide anodes: role of bath composition, analysis of degradation pathways and degradation extent, Sci. Total Environ. 648 (2019) 377–387.
[23] J. De Coster, W. Vanherck, L. Appels, R. Dewil, Selective electrochemical degradation of 4-chlorophenol at a Ti/RuO2-IrO2 anode in chloride rich wastewater, J. Environ. Manag. 190 (2017) 61–71.
[24] F.L. Guzmán-Duque, R.E. Palma-Goyes, I. González, G. Peñuela, R.A. Torres-Palma, Relationship between anode material, supporting electrolyte and current density during electrochemical degradation of organic compounds in water, J. Hazard. Mater. 278 (2014) 221–226.
[25] C. Comninellis, Electrocatalysis in the electrochemical conversion/combustion of organic pollutants for waste water treatment, Electrochim. Acta 39 (1994) 1857–1862.
[26] R. Palma-Goyes, J. Vazquez-Arenas, C. Ostos, A. Manzo-Robledo, I. Romero-Ibarra, J. Calderón, I. González, In search of the active chlorine species on Ti/ZrO2-RuO2-Sb2O3 anodes using DEMS and XPS, Electrochim. Acta 275 (2018) 265–274.
[27] B.N. Grgur, D.Ž. Mijin, A kinetics study of the methomyl electrochemical degradation in the chloride containing solutions, Appl. Catal. B Environ. 147 (2014) 429–438.
[28] F.A. Rodríguez, M.N. Mateo, J.M. Aceves, E.P. Rivero, I. González, Electrochemical oxidation of bio-refractory dye in a simulated textile industry effluent using DSA electrodes in a filter-press type FM01-LC reactor, Environ. Technol. 34 (2013) 573–583.
[29] C. Cheng, G. Kelsall, Models of hypochlorite production in electrochemical reactors with plate and porous anodes, J. Appl. Electrochem. 37 (2007) 1203–1217.
[30] M.R. Cruz-Diaz, E.P. Rivero, F.A. Rodríguez, R. Dominguez-Bautista, Experimental study and mathematical modeling of the electrochemical degradation of dyeing wastewaters in presence of chloride ion with dimensional stable anodes (DSA) of expanded meshes in a FM01-LC reactor, Electrochim. Acta 260 (2018) 726–737.
[31] H. Baltruschat, Differential electrochemical mass spectrometry, J. Am. Soc. Mass Spectrom. 15 (2004) 1693–1706.
[32] S.J. Ashton, Differential electrochemical mass spectrometry, Design, Construction and Research Application of a Differential Electrochemical Mass Spectrometer (DEMS), Springer, 2012 9–27.
[33] R. Palma-Goyes, J. Vazquez-Arenas, C. Ostos, R. Torres-Palma, I. González, The effects of ZrO2 on the electrocatalysis to yield active chlorine species on Sb2O5-doped Ti/RuO2 anodes, J. Electrochem. Soc. 163 (2016) H818–H825.
[34] G. Martelli, R. Ornelas, G. Faita, Deactivation mechanisms of oxygen evolving anodes at high current densities, Electrochim. Acta 39 (1994) 1551–1558.
[35] A. Manzo-Robledo, A.C. Boucher, E. Pastor, N. Alonso-Vante, Electro-oxidation of Carbon Monoxide and Methanol on Carbon-Supported Pt–Sn Nanoparticles: a DEMS Study, Fuel Cells 2 (2002) 109–116.
[36] T. Arikawa, Y. Murakami, Y. Takasu, Simultaneous determination of chlorine and oxygen evolving at RuO2/Ti and RuO2–TiO2/Ti anodes by differential electrochemical mass spectroscopy, J. Appl. Electrochem. 28 (1998) 511–516.
[37] F. Moradi, C. Dehghanian, Addition of IrO2 to RuO2+ TiO2 coated anodes and its effect on electrochemical performance of anodes in acid media, Progr. Nat. Sci.: Materials Int. 24 (2014) 134–141.
[38] Z. Yi, C. Kangning, W. Wei, J. Wang, S. Lee, Effect of IrO2 loading on RuO2–IrO2–TiO2 anodes: A study of microstructure and working life for the chlorine evolution reaction, Ceram. Int. 33 (2007) 1087–1091.
[39] Q. Wang, F. Wu, N. Wang, L. Wang, X. Zhang, Electrochemical behavior of IrxRu1− xO2 oxides as anodic electrocatalyst for electrosynthesis of dinitrogen pentoxide, Electrochim. Acta 74 (2012) 227–234.
[40] P. Liao, Y. Huang, K. Tiong, Characterization of RuO2 and IrO2 films deposited on Si substrate, J. Alloys Compd. 317 (2001) 98–102.
[41] T. Audichon, B. Guenot, S. Baranton, M. Cretin, C. Lamy, C. Coutanceau, Preparation and characterization of supported RuxIr (1-x) O2 nano-oxides using a modified polyol synthesis assisted by microwave activation for energy storage applications, Appl. Catal. B Environ. 200 (2017) 493–502.
[42] H.-Y. Shin, H. Jung, M.H. Kim, S. Yoon, Raman scattering study of IrxRu1− xO2 mixed metal oxide nanowires (0≤ x≤ 1), Curr. Appl. Phys. 14 (2014) S44–S48.
[43] J. Cheng, H. Zhang, G. Chen, Y. Zhang, Study of IrxRu1− xO2 oxides as anodic electrocatalysts for solid polymer electrolyte water electrolysis, Electrochim. Acta 54 (2009) 6250–6256.
[44] R. Erenburg, L. Krishtalik, N. Rogozhina, PH effect on chlorine reaction kinetics on ruthenium titanium oxide anode, Elektrokhimiya 20 (1984) 1183–1190.
[45] M. Murata, T.A. Ivandini, M. Shibata, S. Nomura, A. Fujishima, Y. Einaga, Electrochemical detection of free chlorine at highly boron-doped diamond electrodes, J. Electroanal. Chem. 612 (2008) 29–36.
[46] L. Janssen, L. Starmans, J. Visser, E. Barendrecht, Mechanism of the chlorine evolution on a ruthenium oxide/titanium oxide electrode and on a ruthenium electrode, Electrochim. Acta 22 (1977) 1093–1100.
[47] L.D. Burke, J.F. O'Neill, Some aspects of the chlorine evolution reaction at ruthenium dioxide anodes, J. Electroanal. Chem. Interfacial Electrochem. 101 (1979) 341–349.